Article type: Article

Integrating Ultra-thin Bulk-heterojunction Organic Semiconductor Intermediary for High-performance Low-bandgap Perovskite Solar Cells with Low Energy Loss

Guiying Xu, [a] Pengqing Bi,[c] Shuhui Wang,[a] Rongming Xue,[a] Jingwen Zhang, [a] Haiyang Chen, [a] Weijie Chen, [a] Xiaotao Hao,[c] Yaowen Li, [*a] Yongfang Li [a,b]

Guiying Xu, Shuhui Wang, Rongming Xue, Jingwen Zhang, Haiyang Chen, Weijie Chen, Prof. Yaowen Li,* Prof. Yongfang Li

[a] State and Local Joint Engineering Laboratory for Novel Functional Polymeric Materials, Laboratory of Advanced Optoelectronic Materials, College of Chemistry, Chemical Engineering and Materials Science, Soochow University, Suzhou 215123, China
Prof. Yaowen Li Email: ywli@suda.edu.cn

Prof. Yongfang Li

[b] Beijing National Laboratory for Molecular Sciences; Institute of Chemistry, Chinese Academy of Sciences, Beijing 100190, China

Prof. Xiaotao Hao, Pengqing Bi

[c] School of Physics and State Key Laboratory of Crystal Materials, Shandong University, Jinan, Shandong 250100, China

Keywords: Sn-Pb perovskite solar cells; low bandgap; energy loss; high open-circuit voltage; Bulk-heterojunction organic semiconductor

Abstract

Mixed tin (Sn)–lead (Pb) perovskite is considered the most promising low-bandgap photovoltaic material for both pursuing the theoretical limiting efficiency of single-junction solar cells and breaking the Shockley–Queisser limitation by constructing tandem solar cells. However, their power conversion efficiencies (PCEs) are still lagging behind those of medium-bandgap perovskite solar cells (pero-SCs) due to their serious energy loss (E_{loss}). In this work, we used an ultra-thin bulk-heterojunction (BHJ) organic semiconductor (PBDB-T:ITIC) layer as an intermediary between the hole transporting layer and Sn–Pb-based low-bandgap perovskite film to minimize E_{loss}. It was found that this BHJ PBDB-T:ITIC intermediary simultaneously provided a cascading energy alignment in the device, facilitated high-quality Sn–Pb perovskite film growth, and passivated the antisite defects of the perovskite surface. In this simple way, the E_{loss} of pero-SCs based on $(FASnI_3)_{0.6}(MAPbI_3)_{0.4}$ (bandgap $\approx$ 1.25 eV) was dramatically reduced below 0.4 eV, leading to a high open-circuit voltage (V_{oc}) of 0.86 V. As a result, the best pero-SC showed a significantly improved PCE of 18.03% with negligible J–V hysteresis and high stability. To the best of our knowledge, the PCE of 18.03% and V_{oc} of 0.86 V are the highest values among the low-bandgap pero-SCs to date.

1. Introduction

The recently emerged organic-metal halide perovskite solar cells (pero-SCs), with the formula ABX_3 (where A is a monovalent cation, B is a metal cation, and X is a halide anion), have been one of the most rapidly developed types of solar cells.[1-6] Lead (Pb)-based perovskite materials with a

medium bandgap of approximately 1.55 Ev[7] are the most efficient pero-SCs, with power conversion efficiencies (PCEs) exceeding 22%.[8-9] However, the heavy metal Pb is not ecofriendly, [10-12] and a PCE beyond 22% is close to the single-junction Shockley–Queisser (SQ) limit for medium-bandgap perovskite-based devices. [13] The maximum theoretical efficiency of a single-junction device could be increased to over 30% by reducing the perovskite bandgap to ~1.2 eV. [13] In addition, perovskite–perovskite tandem solar cells consisting of a bottom cell with a bandgap of 0.9–1.3 eV and a top cell with a bandgap of 1.7–1.9 eV can also be used to improve efficiency beyond the S–Q limit in single-junction solar cells. [14-15] Therefore, it is highly desirable to develop high-performance perovskite materials with low bandgaps and toxicity.

The replacement of Pb^{2+} with tin (Sn^{2+}) has been regarded as one of the most promising strategies to reduce bandgap, and the nontoxic Sn can significantly decrease Pb content, providing a more environmentally friendly perovskite material. In 2014, Kanatzidis and co-workers reported a Sn-completely-substituted perovskite $CH_3NH_3SnI_3$ showing a low bandgap of 1.3 eV. [16] Interestingly, the bandgap was further reduced to 1.1 eV by a mixed Sn–Pb perovskite due to their tunable bandgaps by varying the Sn:Pb ratio. [12] Such a low-bandgap perovskite film can extend their absorption to the near-infrared region, enabling the absorption of more solar photons. In addition to the ideal bandgap of Sn–Pb perovskite, its high optical absorption coefficient and low exciton binding energies indicate it is a good candidate as a photoactive layer material for high-performance pero-SCs. [17-18] However, the efficiency of low-bandgap pero-SCs is still far behind those of medium-bandgap pero-SCs, particularly for Pb-based devices (e.g., $CH_3NH_3PbI_3$).

In previous work, tremendous efforts were devoted to developing high-quality, uniform, and fully covered Sn–Pb perovskite films by additives and solvent engineering methods for improving

their photovoltaic performance. [19-25] However, the performance is still limited by severe energy loss (E_{loss}) from photovoltage loss ($E_{loss} = E_g - eV_{oc}$). [26] As seen from the E_{loss} statistics of efficient Pb-Sn-based pero-SCs in **Figure 1**a and Table S1 in the Supporting Information, almost all of them show E_{loss} values as high as above 0.5 eV. There are two possible reasons for the high E_{loss}. On the one hand, the low valence band (E_V) of low-bandgap perovskite film usually has a big band alignment mismatch with the highest occupied molecular orbital (HOMO) or valence band (VB) of the conventional hole transporting layer (HTL). On the other hand, the prevailing trap-state density and poor morphology of Sn–Pb perovskite films may cause serious charge carrier recombination. [27] Recently, Yan et al. developed a thick Sn–Pb low-bandgap (1.25 eV) perovskite film (~600 nm) with large grains and high crystallinity, which could dramatically enhance carrier lifetimes. The pero-SC with this favorable perovskite film showed a $V_{oc,loss}$ as low as 0.40 V, thus leading to the highest reported PCE of 17.6% in low-bandgap pero-SCs. [19] However, the carrier lifetimes of thick perovskite layers critically depend on their grain sizes and crystallinity, which makes it more difficult to control the growth of Sn–Pb perovskite films. Jen et al. used $IC_{60}BA$ to replace C_{60} as an electron transporting layer for optimizing the band alignment of low-bandgap pero-SC, [27] thus delivering a significantly improved E_{loss}. However, its unfavorable fill factor (FF) of 67% and short-circuit current density (J_{sc}) of 25.5 mA/cm^2 resulted in an unsatisfactory PCE of 14.4%. It was probably caused by the high trap-state density existing in the perovskite film, which seemed to be a consequence of the poor morphology of the perovskite film grown on hydrophilic PEDOT:PSS and the lower trap-state density passivation effect of $IC_{60}BA$. Recently, the deep trap-state density and surface defects formed on the surface of perovskite crystals were demonstrated to serve as a strong charge recombination center, which

greatly affected the E_{loss} of a device.[28-29] Therefore, both the mismatch band alignment and high trap-state density in low-bandgap perovskite film seriously limit their related device performance.

To overcome these challenges, we used an ultra-thin bulk-heterojunction (BHJ) organic semiconductor (PBDB-T:ITIC) layer [30] (Figure 1b) as an intermediary between the HTL PEDOT:PSS and low-bandgap (1.25 eV) $(FASnI_3)_{0.6}(MAPbI_3)_{0.4}$ film. This BHJ PBDB-T:ITIC intermediary has step-elevated HOMO energy levels and an efficient exciton dissociation/transport ability, so it can form a gradient band alignment and charge transport channel efficiently. Importantly, this ultra-thin PBDB-T:ITIC intermediary can facilitate the growth of high-quality $(FASnI_3)_{0.6}(MAPbI_3)_{0.4}$, and the CN and O atoms in PBDB-T:ITIC can effectively passivate the surface trap-state density of perovskite film. As a result, the low-bandgap pero-SCs with a structure of ITO/PEDOT:PSS/PBDB-T:ITIC/$(FASnI_3)_{0.6}(MAPbI_3)_{0.4}$ (310 nm)/C_{60}/2,9-dimethyl-4,7-diphenyl-1,10-phenanthroline (BCP)/Ag showed a promising PCE of 18.03% with negligible J-V hysteresis and a small E_{loss} of 0.39 eV. As shown in Table S1, 18.03% is the highest reported PCE in the low-bandgap pero-PCs to date. Moreover, these devices also exhibited substantial enhancement in both reproducibility and stability.
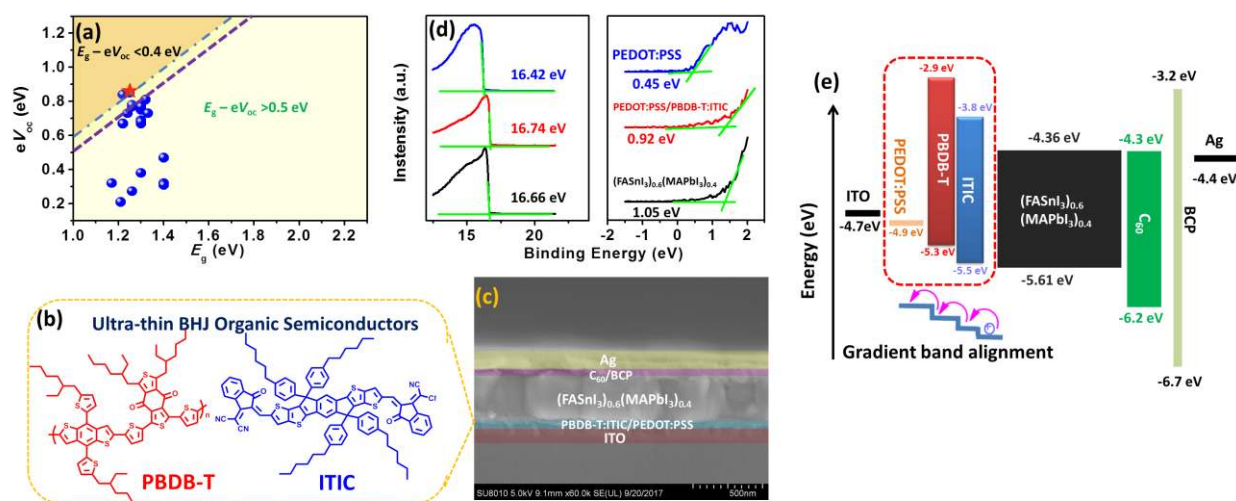
2. Results and discussion

Figure 1. (a) Plots of eV_{oc} against E_g for Sn or Sn–Pb-based low-bandgap (below 1.4 eV) pero-SCs reported so far (eV_{oc} and E_g values cited from literature). (b) Chemical structures of PBDB-T and ITIC; (c) Cross-section SEM image of *p-i-n* pero-SC; (d) UPS measurements for PEDOT:PSS, PEDOT:PSS/PBDB-T:ITIC, and $(FASnI_3)_{0.6}(MAPbI_3)_{0.4}$ films: Left: photoemission cutoff spectra; Right: Valence band structure of PEDOT:PSS, PEDOT:PSS/PBDB-T:ITIC, and $(FASnI_3)_{0.6}(MAPbI_3)_{0.4}$ films; (e) Energy-level diagram of pero-SCs and HOMO and LUMO energy levels of PBDB-T:ITIC (cited from literature).[30]

We fabricated the low-bandgap pero-SC with a *p-i-n* structure of ITO/PEDOT:PSS/PBDB-T:ITIC/$(FASnI_3)_{0.6}(MAPbI_3)_{0.4}$/$C_{60}$/BCP/Ag, where the bandgap of $(FASnI_3)_{0.6}(MAPbI_3)_{0.4}$ was determined to be approximately 1.25 eV by fitting the $(\alpha h\upsilon)^2$-E plot of a perovskite film as shown in Figure S1 (Supporting Information). The PBDB-T:ITIC dilute solution (3 mg/mL) was spin-coated on top of PEDOT:PSS at a high speed (6000 rpm), resulting in a 15-nm-thick PBDB-T:ITIC blend film. Such an ultra-thin film can be well maintained even after coating with subsequent $(FASnI_3)_{0.6}(MAPbI_3)_{0.4}$ film. Because the pristine PBDB-T:ITIC films before and after washing with DMF:DMSO solvent show consistent S2p peaks of X-ray photoelectron spectroscopy (XPS) (Figure S2, Supporting information), which was attributed to the thiophene moieties in PBDB-T:ITIC film. Note that the DMF:DMSO is

exactly the same as sovlent of $(FASnI_3)_{0.6}(MAPbI_3)_{0.4}$ precursor solution. This ultra-thin intermediary plays an essential role in optimizing device band alignment and perovskite film growth. To determine the exact band structures of PEDOT:PSS, PEDOT:PSS/PBDB-T:ITIC, and $(FASnI_3)_{0.6}(MAPbI_3)_{0.4}$, we carefully characterized them using ultraviolet photoelectron spectroscopy (UPS). As shown in Figure 1d (left), the ultra-thin PBDB-T:ITIC intermediary significantly elevated the work function (W_S) of PEDOT:PSS from -4.90 to -4.48 eV, indicating that the BHJ PBDB-T:ITIC could induce a higher hole density. [31] The increased hole density is ascirbed to the electrons transfer from PBDB-T to ITIC and hole transfer from PEDOT:PSS to PBDB-T:ITIC layer that would leave more hole in Ev of PEDOT:PSS/PBDB-T:ITIC film, thus enable to reduce charge recombination in the HTL. [32] This behavior was further demonstrated by the capacitance-voltage measurement of related devices. As shown in Figure S3 (Supporting Information), the carrier concentration (N_A) can be calculated to be 4.41×10^{16} cm^{-3} and 7.34×10^{16} cm^{-3} for the device without and with PBDB-T:ITIC, respectively. The increased N_A may attribute to the above combination effect that would facilitate charge transport. Combining the similar hole mobilities of PEDOT:PSS (2.20×10^{-5} $cm^2/V \cdot s$) and PEDOT:PSS/PBDB-T:ITIC (1.81×10^{-5} $cm^2/V \cdot s$) (Figure S4 and Table S2, Supporting Information), this additional PBDB-T:ITIC intermediary with high hole density would enhance the hole conductivity of the HTL. The conduction band (E_C) and E_v of the $(FASnI_3)_{0.6}(MAPbI_3)_{0.4}$ film as obtained from $E_C = W_S + VBM - E_g$ and $E_V = W_S + VBM$[33] were -4.36 eV and -5.61 eV, respectively. As shown in Figure 1e, the E_V of $(FASnI_3)_{0.6}(MAPbI_3)_{0.4}$ was close to the HOMOs of PBDB-T and ITIC, and it formed a gradient band alignment between $(FASnI_3)_{0.6}(MAPbI_3)_{0.4}$ and PEDOT:PSS. This result can be further confirmed by the E_V of PBDB-T:ITIC (-5.4 eV) lying between the W_S of PEDOT:PSS and E_V of $(FASnI_3)_{0.6}(MAPbI_3)_{0.4}$. Taken together with the high hole conductivity of PBDB-T:ITIC, it provided a fluent hole transport

7

path from the perovskite film to the anode. In addition, the high-lying LUMO energy levels of both PBDB-T (-2.9 eV) and ITIC (-3.8 eV) effectively blocked electrons from recombining with holes at the interface of PBDB-T:ITIC/perovskite.
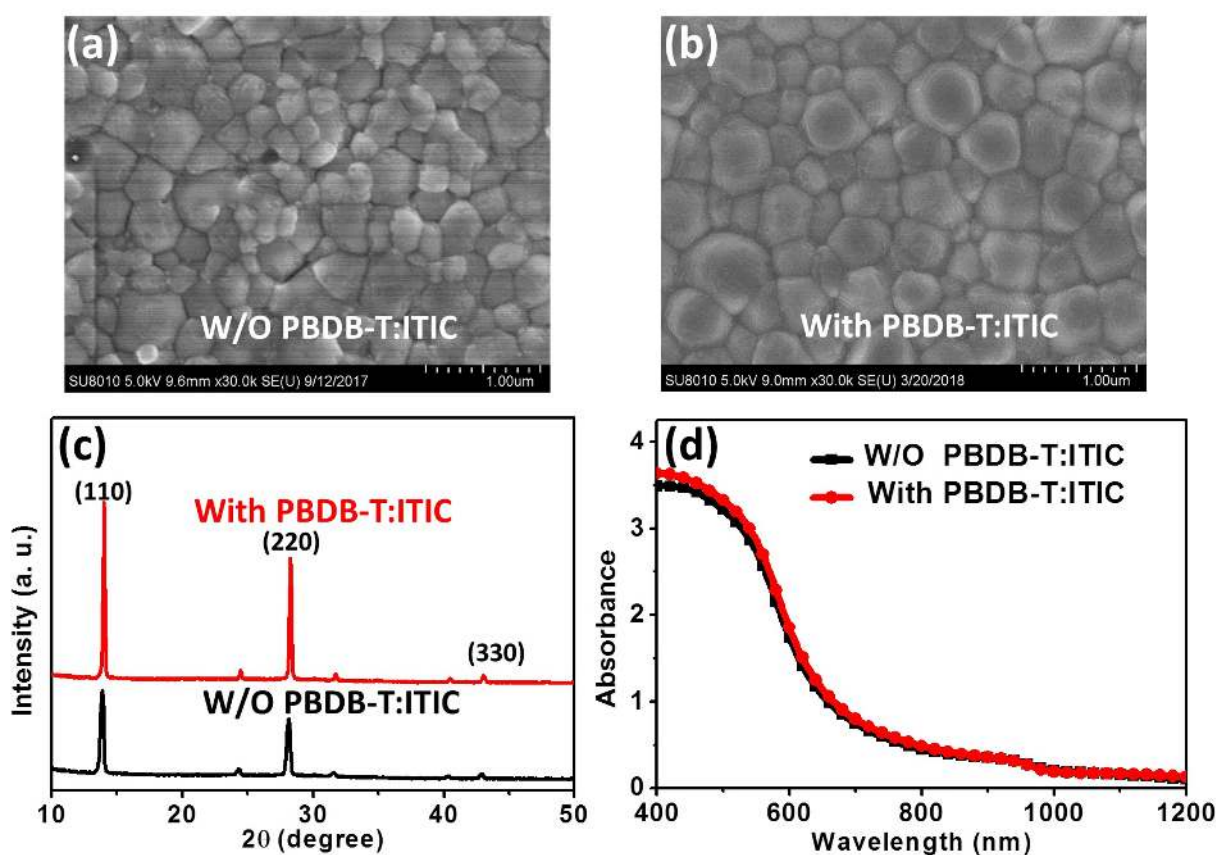

Figure 2. Top-view SEM images of $(FASnI_3)_{0.6}(MAPbI_3)_{0.4}$ films grown on (a) PEDOT:PSS and (b) PEDOT:PSS/PBDB-T:ITIC; (c) XRD patterns of $(FASnI_3)_{0.6}(MAPbI_3)_{0.4}$ films grown on PEDOT:PSS and PEDOT:PSS/PBDB-T:ITIC; (d) UV-Vis absorption spectra of $(FASnI_3)_{0.6}(MAPbI_3)_{0.4}$ film grown on PEDOT:PSS and PEDOT:PSS/PBDB-T:ITIC.

The growth of perovskite film is heavily dependent on the underlying layer's physical properties, such as its roughness and wettability. Atomic force microscopy (AFM) images revealed that both the

PEDOT:PSS and PBDB-T:ITIC-coated PEDOT:PSS showed uniform surface and low roughness (root-mean-square in the range of 3.05–3.56 nm) (Figure S5a, Supporting Information). However, the surface wettability changed obviously, as observed from the significantly increased water contact angles from 6.33° to 95.60° due to the incorporation of the hydrophobic PBDB-T:ITIC organic intermediary (Figure S5b, Supporting Information). This hydrophobic surface would greatly affect the consequent perovskite film growth. [34-35] As shown in **Figure 2**a-b, the $(FASnI_3)_{0.6}(MAPbI_3)_{0.4}$ film grown on this hydrophobic and smooth PBDB-T:ITIC intermediary showed a more compact and larger grain size than that grown on PEDOT:PSS (W/O PBDB-T:ITIC). This variation can also be clearly observed from the statistics of grain size distribution showing a homogeneous distribution and significantly increased average grain sizes (from 282 nm to 441 nm) (Figure S6, Supporting Information). As seen from the cross-section scanning electron microscopy (SEM) of the whole device (Figure 1c), this compact and large grain $(FASnI_3)_{0.6}(MAPbI_3)_{0.4}$ can even uniformly expand to several micrometers along the substrate, resulting in perpendicular and negligible grain boundaries, which can effectively minimize the grain-boundary energy and trap-state density, as demonstrated previously. [36-37]

The quality of $(FASnI_3)_{0.6}(MAPbI_3)_{0.4}$ films was further evaluated by X-ray diffraction (XRD) analysis. As shown in Figure 2c, the $(FASnI_3)_{0.6}(MAPbI_3)_{0.4}$ films grown on PBDB-T:ITIC showed stronger and sharper (110) and (220) characteristic peaks compared with those grown on PEDOT:PSS (W/O PBDB-T:ITIC), indicating a pure phase and higher crystallinity. The related narrower full width at half-maximum (FWHM) of the (110) peak (0.16°) again demonstrated an increased grain size, which is consistent with the results obtained from SEM images. [19] We also noted that the two absorption spectra of the $(FASnI_3)_{0.6}(MAPbI_3)_{0.4}$ films were almost the same in terms of both shape

and intensity (Figure 2d), although the additional ultra-thin PBDB-T:ITIC intermediary reduced the transmittance to a certain extent in the visible region (Figure S7, Supporting Information). This result suggests that the enhanced quality of the $(FASnI_3)_{0.6}(MAPbI_3)_{0.4}$ film contributes to its absorption ability.
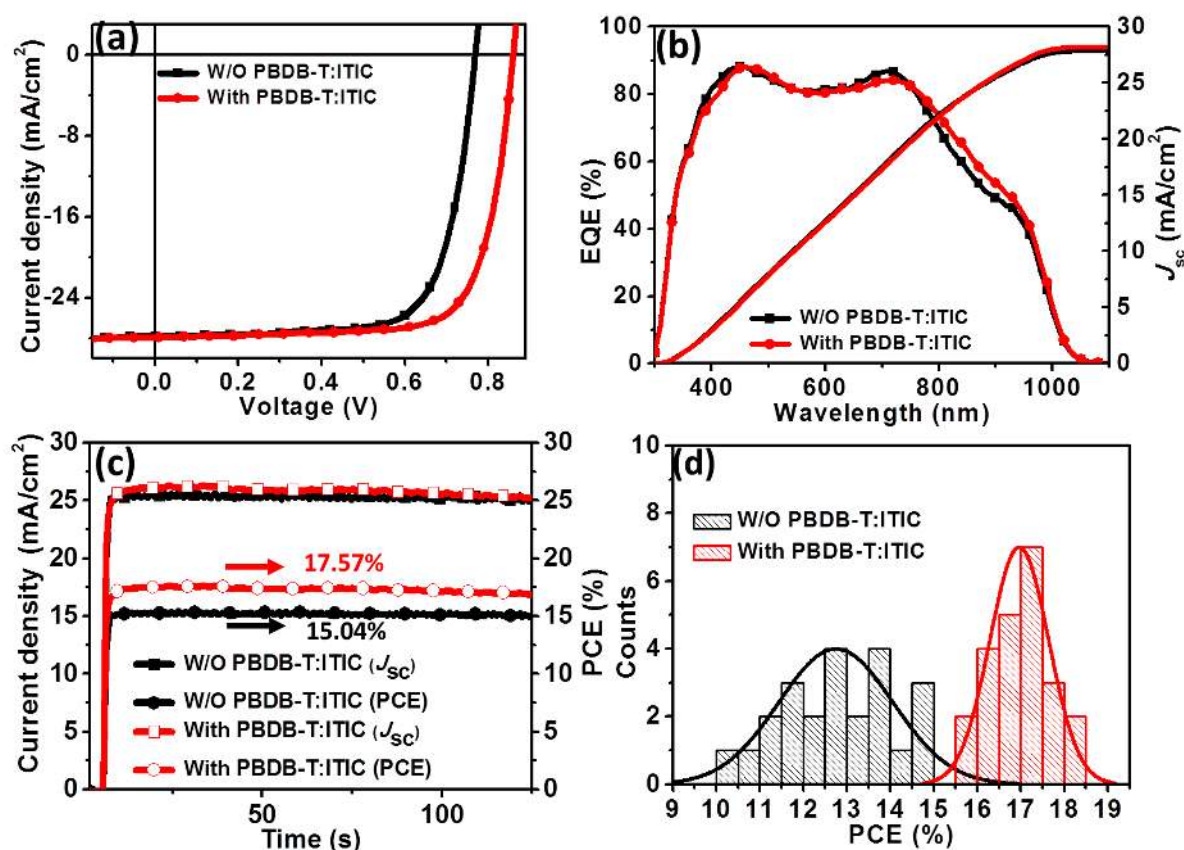

Figure 3. (a) *J-V* curves of pero-SCs under illumination of AM1.5G 100 mW/cm^2; (b) EQE spectra of corresponding pero-SCs. (c) Maximal steady-state photocurrent output of champion devices at maximum power point (at 0.61 V for the pero-SCs without PBDB-T:ITIC, at 0.69 V for the pero-SCs with PBDB-T:ITIC, and their corresponding output power). (d) Device performance distribution for 23 devices in one batch.

Table 1. Summary of Photovoltaic Parameters of Pero-SCs With or Without PBDB-T:ITIC.

10

Devices	V_{oc} (V)	J_{sc} (mA/cm^2)	FF (%)	PCE[a] (%)	PCE (%)[b] max. power output
W/O PBDB-T:ITIC (RS)	0.75±0.03 (0.77)	27.52± 0.70 (27.82)	0.70±0.04 (0.72)	14.50± 0.80 (15.41)	15.17
W/O PBDB-T:ITIC (FS)	0.75±0.03 (0.76)	27.22± 0.75 (27.42)	0.69±0.05 (0.72)	14.02± 0.90 (15.00)	
With PBDB-T:ITIC (RS)	0.84±0.02 (0.86)	27.60± 0.60 (27.92)	0.73±0.01 (0.751)	17.79± 0.40 (18.03)	17.57
With PBDB-T:ITIC (FS)	0.82±0.02 (0.85)	27.60± 0.63 (27.90)	0.72±0.02 (0.74)	17.15± 0.50 (17.55)	

[a] Average and standard deviation values were obtained based on 20 cells from 3 different batches for each active layer. Parameters of the best cell are reported in brackets. FS: forward scan, scan rate 200 mV/s, delay time 100 ms; RS: reverse scan, scan rate 200 mV/s, delay time 100 ms. [b] Maximal steady-state power output, which equals the PCE of maximum power output.

Figure 3a shows the current density–voltage *(J-V)* characteristics of low-bandgap pero-SC with or without ultra-thin PBDB-T:ITIC intermediary, measured under the illumination of AM1.5G 100 mW/cm^2. The detailed photovoltaic parameters are listed in **Table 1**. The control device (W/O PBDB-T:ITIC) gave a short-circuit current density (J_{sc}) of 27.82 mA/cm^2, an open-circuit voltage (V_{oc}) of 0.77 V, an FF of 72.0%, and a PCE of 15.42%, which are comparable with the previous results. [38] When employing ultra-thin PBDB-T:ITIC intermediary on top of PEDOT:PSS, the related device performance was significantly enhanced, showing a J_{sc} of 27.92 mA/cm^2, a V_{oc} of 0.86 V, an FF of 75.1%, and a PCE of 18.03%. Importantly, both the 18.03% PCE and 0.86 V V_{oc} are the highest values among the reported Sn–Pb-based low-bandgap pero-SCs to date. It should be pointed out that this high V_{oc} value led to a great breakthrough in the performance of low-bandgap pero-SC systems. The external quantum efficiency (EQE) spectra of both pero-SCs (Figure 3b) demonstrated integrated J_{sc} values (28.21 mA/cm^2 and 27.95 mA/cm^2) that agreed well with those obtained from *J-V* curves. Meanwhile, as shown in Figure 3c, the maximal steady-state PCEs exhibited values close to those of their related PCEs obtained from *J-V* curves at reverse scan, delivering 15.04% for the control device (W/O PBDB-T:ITIC) and 17.57% for the devices with PBDB-T:ITIC. Moreover, the pero-SCs also showed almost coincident reverse and forward scan *J-V* curves (Figure S8, Supporting Information), which firmly confirmed that the Sn–Pb low-bandgap pero-SCs had weak hysteresis behavior without being influenced by the inserted ultra-thin PBDB-T:ITIC intermediary. Figure 3d shows the histogram of the PCE values of 23 devices with or without ultra-thin PBDB-T:ITIC. As shown, nearly 90% of the devices with PBDB-T:ITIC delivered PCEs over 16.5%, while the control devices only showed PCEs of 11.0% on average. This substantially enhanced device efficiency and reproducibility indicate that incorporating ultra-thin PBDB-T:ITIC intermediary is a promising method for achieving high-performance Sn–Pb-

based low-bandgap pero-SCs. In addition, the stability of the pero-SCs without encapsulation was investigated in a nitrogen atmosphere. As shown in Figure S9 (Supporting Information), the stability of pero-SC with PBDB-T:ITIC was significantly improved, in that 80% of the initial PCE was maintained after 600 hours, while the PCE of pero-SC without PBDB-T:ITIC degraded to 31%. This behavior could be due to the hydrophobic PBDB-T:ITIC intermediary effectively encapsulating the underlying acidic PEDOT:PSS HTL and preventing it from reacting with the perovskite film. [39]

Considering the overall improved device performance, we then systematically investigated the effect of this ultra-thin BHJ organic semiconductor intermediary on the charge dynamics in the devices. Firstly, the plots of photocurrent (J_{ph}) versus the effective applied voltage (V_{eff}) for the devices with and without PBDB-T:ITIC were measured to comprehensively study the influence of PBDB-T:ITIC on the exciton dissociation and charge collection properties of the devices (**Figure 4**a).[40-41] The control device without PBDB-T:ITIC showed a $J_{ph}/J_{ph,sat}$ of 95.39%, suggesting that unfavorable exciton dissociation efficiency and ineffective charge transport existed in the pero-SC. By contrast, the device with PBDB-T:ITIC gave a high $J_{ph}/J_{ph,sat}$ of 99.16%, demonstrating that this ultra-thin intermediary provided efficient charge transport channels for collecting holes. One possible reason is that PBDB-T:ITIC constructed an intermediary with a gradient band alignment and high hole density between the low-bandgap perovskite and anode, which effectively reduced the hole transport barrier. Another possible reason is that the improved perovskite quality and trap-state density passivation effect existed at the interfaces or in the perovskite film. In addition, we also investigated the hole mobilities of whole devices by SCLC method. The measurement results are shown in Figure S10 and Table S3 in Supporting Information. It is clear that the device with PBDB-

T:ITIC has a higher mobility (6.63×10^{-2} cm^2/V•s) than that of device without PBDB-T:ITIC (4.39×10^{-2} cm^2/V•s).
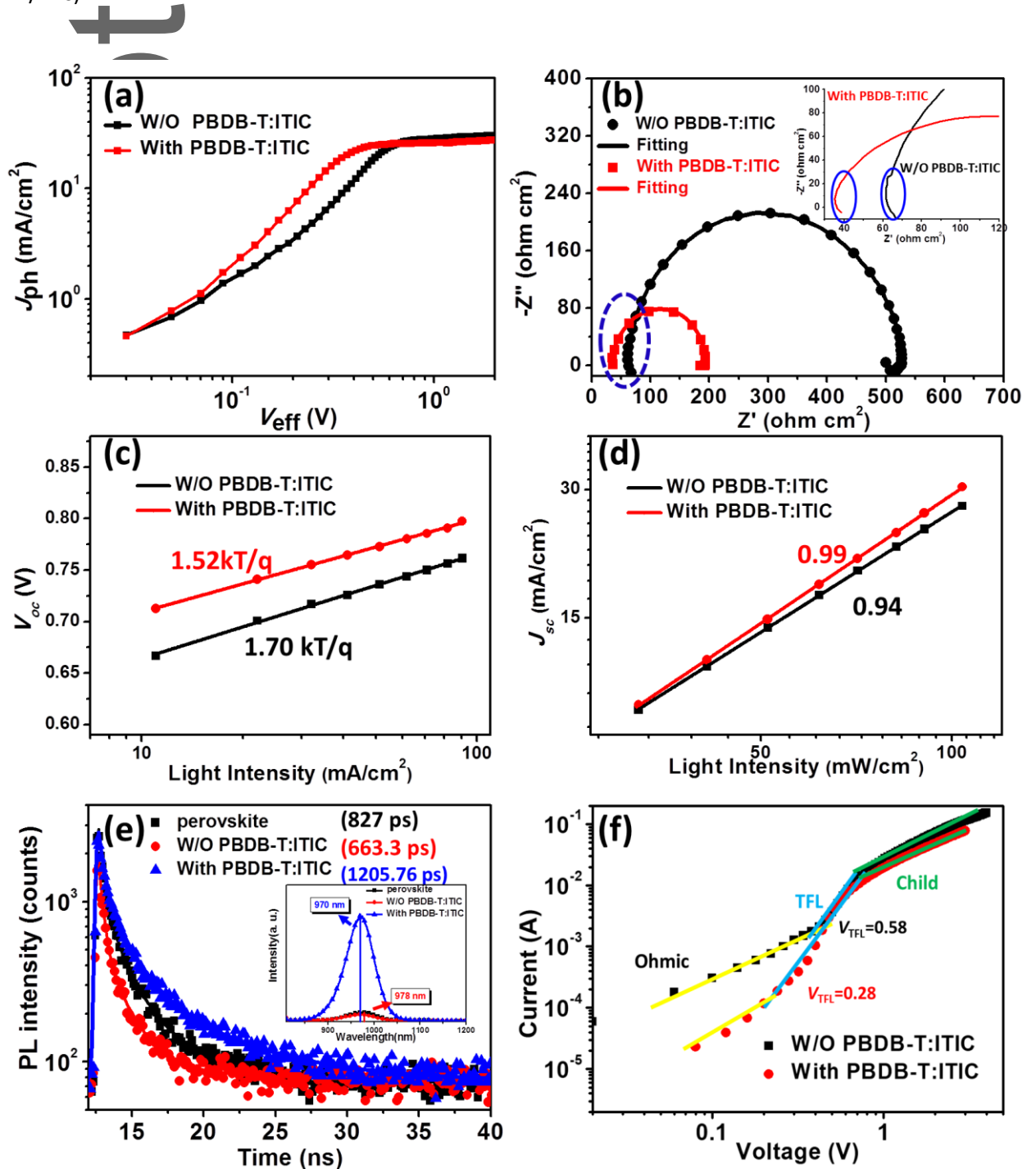
Figure 4. (a) Charge collection probability as function of internal voltage. (b) Nyquist plots (symbols) and fitting curves (solid lines) of alternating current IS of pero-SCs. Alternating current IS values were measured at a voltage close to V_{oc}. Inset: magnified view in high frequency region. (c) J_{sc} and (d) V_{oc} as function of light intensity for pero-SCs. (e) Normalized TRPL decay transient spectra of $(FASnI_3)_{0.6}(MAPbI_3)_{0.4}$ grown on glass, PEDOT:PSS, and PEDOT:PSS/PBDB-T:ITIC. Inset: the related Steady-state PL spectra. (f) Hole-only devices for direct measurement of trap-state density.

To verify these speculations, we carried out alternating current impedance spectroscopy (IS) measurements to understand the charge extraction and recombination processes in the devices, as shown in Figure 4b. The fitted equivalent circuit of the devices are shown in Figure S11, where the equivalent circuit is composed of series resistance (R_s), charge transfer resistance (R_{CT}) at interfaces, and recombination resistance (R_{rec}) inside the perovskite film forming a parallel circuit with capacitor C (C_{CT} and C_{rec}).[42-44] The corresponding parameters are shown in Table S4 of Supporting Information. It can be seen that the R_{CT} is obviously reduced from 357.3 Ω cm^2 to 34.74 Ω cm^2 after incorporating PBDB-T:ITIC, which clearly demonstrates that the PBDB-T:ITIC intermediary with the gradient band alignment and high hole density in the device is in favor of hole extraction/transport. Moreover, we noted that the ultra-thin PBDB-T:ITIC intermediary also significantly affected the charge recombination, which led to a dramatically increased R_{rec} from 100.2 Ω cm^2 to 208.5 Ω cm^2. The larger R_{rec} value suggests a slower charge recombination rate, which probably originates from the reduced trap-state density in the perovskite film or at interfaces.

To gain more insight into the effect of PBDB-T:ITIC intermediary on the trap-state density in devices, we measured the dependence of J_{sc} and V_{oc} on various light intensities (P_{light}), giving the relationships of $J_{sc} \propto P_{light}^{\alpha}$ and $V_{oc} \propto (nkT/q)\ln(P_{light})$. Under short-circuit conditions, the device with PBDB-T:ITIC showed a slightly increased α value (0.99) closer to unity compared to that (0.94) of the

device without PBDB-T:ITIC (Figure 4c). This result indicated that almost all free carriers in the device with PBDB-T:ITIC were swept out and collected at the electrodes prior to bimolecular recombination owing to the favorable band alignment and efficient coupling interface,[45] which consequently contributed to an improvement of FF. In contrast, under open-circuit conditions, all photogenerated free carriers recombine, and the slope of V_{oc} versus light intensity is equal to kT/q if bimolecular recombination dominates.[46] However, as shown in Figure 4d, both the devices with and without PBDB-T:ITIC showed obviously deviated slopes from $1kT/q$, suggesting that additional Shockley–Read–Hall (SRH) recombination had occurred, in which electrons and holes recombined through trap sites in the perovskite film.[45] Therefore, the smaller slope (n=1.52) of the device with PBDB-T:ITIC suggests reduced SRH recombination owing to the low trap-state density in the low-bandgap $(FASnI_3)_{0.6}(MAPbI_3)_{0.4}$. This behavior was further confirmed by the significantly enhanced steady-state photoluminescence (PL) intensity (more than one order of magnitude, inset of **Figure 4**e) and prolonged average recombination lifetime ($\tau_{average}$) (almost 1.5 times longer, Figure 4e) compared to those of perovskite film grown on PEDOT:PSS (W/O PBDB-T:ITIC). The corresponding parameters are summarized in Table S5 (Supporting Information).

It is noteworthy that the $(FASnI_3)_{0.6}(MAPbI_3)_{0.4}$ grown on glass and PEDOT:PSS (W/O PBDB-T:ITIC) had the same PL peak at 978 nm, while the perovskite film grown on PBDB-T:ITIC triggered a slight blueshift of the PL peak from 978 to 970 nm (inset of Figure 4e). Such a 8-nm-blueshift PL peak could be ascribed to the trap-state density passivation effect originating from PBDB-T:ITIC organic molecules.[47] To quantify the reduced trap-state density at the interface of perovskite films, we calculated the trap density (n_t) according to the equation of $n_t = \dfrac{V_{TFL}\varepsilon\varepsilon_0}{eL^2}$ by space charge limited

current (SCLC) measurement, where the device structure was ITO/PEDOT:PSS/PBDB-T:ITIC (with or without)/$(FASnI_3)_{0.6}(MAPbI_3)_{0.4}$/MoO$_3$/Ag.[48-51] As shown in Figure 4f, the J-V curves of the devices on a double logarithmic scale included three regions of behavior: the Ohmic region, the trap-filled limit (TFL) region, and the child region. The V_{TFL} (onset voltage of TFL region) of the pero-SC without PBDB-T:ITIC was 0.58 V, leading to a trap-state density of 8.99×10^{15} cm^{-3}. After incorporating PBDB-T:ITIC, the V_{TFL} was reduced to 0.28 V, leading to a decreased hole trap-state density of 4.34×10^{15} cm^{-3}. This result directly confirmed that PBDB-T:ITIC can effectively reduce the hole trap-state density of a perovskite film's surface via the intermolecular electronic coupling between $(FASnI_3)_{0.6}(MAPbI_3)_{0.4}$ and PBDB-T:ITIC. Efficient electronic coupling is a precondition of efficient charge transport from perovskite to respective electrodes. As a result, the pero-SC with PBDB-T:ITIC showed a dramatically reduced E_{loss} from 0.51 eV to 0.39 eV, which is one of the smallest reported E_{loss} in the low-bandgap pero-SCs (Figure 1a).

Considering the critical role of the surface trap-state density passivation effect of perovskite film in reducing the E_{loss} of pero-SC, we further investigate how the ultra-thin PBDB-T:ITIC intermediary passivates the $(FASnI_3)_{0.6}(MAPbI_3)_{0.4}$ surface by using the density functional theory (DFT) and Raman spectra. According to the previous report, the trap-state density is severely dependent on the structural stability and electronic states of the representative (110) and (001) surfaces of perovskite crystals, particularly for the (001) surface.[52] As shown in **Figure 5**a, the optimized geometry structures of $(FASnI_3)_{0.6}(MAPbI_3)_{0.4}$ revealed that the antisite defect sites, known as deep-level defects, which are the most detrimental defects in pero-SCs, prevailed in the perovskite film.[53] The density distribution plots of the $(FASnI_3)_{0.6}(MAPbI_3)_{0.4}$ (001) surface showed that the electron distribution was localized around the antisite defect site (Figure 5b), which can capture charge

carriers and induce charge recombination.[54] However, this electron distribution of $(FASnI_3)_{0.6}(MAPbI_3)_{0.4}$ became more delocalized during contact with ITIC molecules, suggesting that the localized states were passivated (Figure 5c), because the CN group in ITIC could bond to Sn atoms (CN-Sn: 2.51 Å) that could effectively passivate the antisite defects of $(FASnI_3)_{0.6}(MAPbI_3)_{0.4}$. In addition, as shown in Figure 5d, the $(FASnI_3)_{0.6}(MAPbI_3)_{0.4}$ grown on PBDB-T:ITIC showed a dramatically enhanced intensity of the Raman band at 70 cm^{-1} (70 cm^{-1} is assigned to O–Pb stretching) compared to that grown on PEDOT:PSS. It revealed that O atoms in PBDB-T and ITIC can also form O–Pb bonds and thus further passivate the surface defects of perovskite film, which is consistent with the result reported by Li et al.[28] A clear molecular interaction between PBDB-T:ITIC and $(FASnI_3)_{0.6}(MAPbI_3)_{0.4}$ is illustrated in Figure 5e.

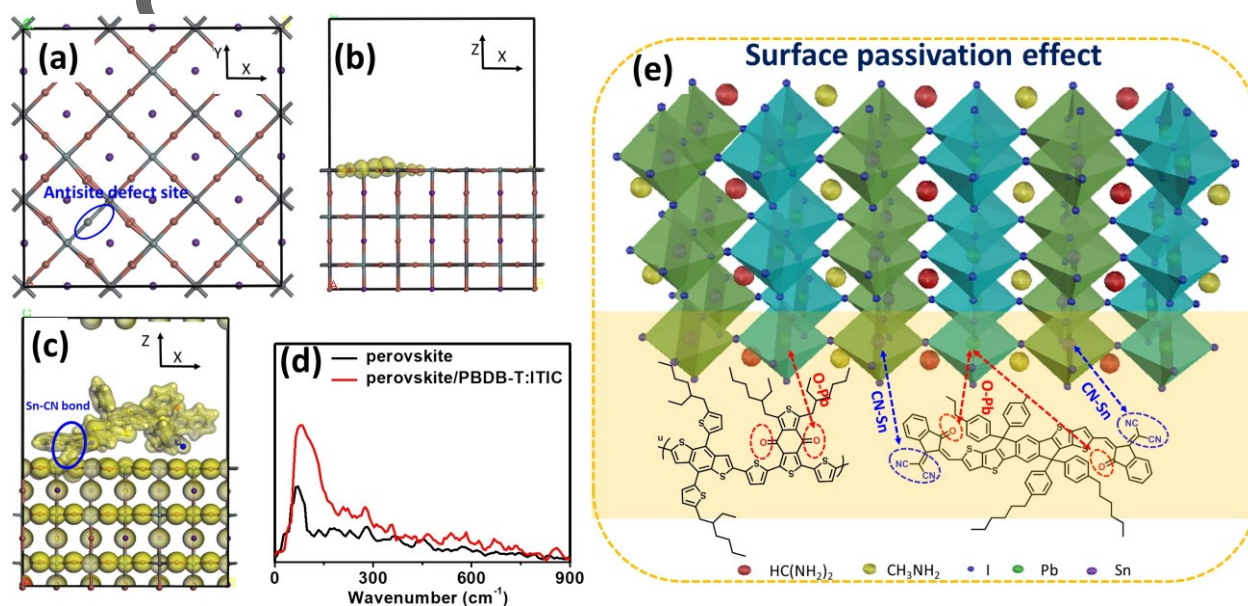**Figure 5.** (a) Atomic configuration of $(FASnI_3)_{0.6}(MAPbI_3)_{0.4}$. Density distribution plots of (b) $(FASnI_3)_{0.6}(MAPbI_3)_{0.4}$ (001)-surface and (c) ITIC on 110-surface with antisite defects. (d) Raman spectra of the $(FASnI_3)_{0.6}(MAPbI_3)_{0.4}$ grown on the PEDOT:PSS or PBDB-T:ITIC. (d) Schematic of surface passivation effect on $(FASnI_3)_{0.6}(MAPbI_3)_{0.4}$ film.

3. Conclusion

In summary, we developed a simple way to address the bottleneck of the high E_{loss} of low-bandgap pero-SCs by incorporating an ultra-thin BHJ organic semiconductor (PBDB-T:ITIC) layer as an intermediary between the HTL and $(FASnI_3)_{0.6}(MAPbI_3)_{0.4}$ film. The hydrophobic PBDB-T:ITIC intermediary was demonstrated to have multi-functionality in fabricating high-performance low-bandgap pero-SCs. That is, it constructed a gradient band alignment in the device, formed high-quality $(FASnI_3)_{0.6}(MAPbI_3)_{0.4}$ film, and had a passivation effect on the surface trap-state density of perovskite film. These synergistic effects can provide efficient charge transport channels for collecting holes, thus dramatically reducing the E_{loss} in low-bandgap pero-SCs. As a result, the optimized device showed a promising PCE of 18.03% with negligible *J-V* hysteresis behavior and a breakthrough V_{oc} of up to 0.86 V accompanied by an E_{loss} as low as 0.39 eV. The PCE of 18.03% is the highest reported value in the low-bandgap (below 1.4 eV) pero-PCs to date. Moreover, these devices also exhibited substantial enhancement in both reproducibility and stability. This study offers an effective protocol for further breakthroughs in the PCEs of both single-junction and tandem pero-SCs.

WILEY-VCH

References

[1]   A. Kojima, K. Teshima, Y. Shirai, T. Miyasaka, *J. Am. Chem. Soc.* **2009***, 131,* 6050*.*

[2]   J. Burschka, N. Pellet, S.-J. Moon, R. Humphry-Baker, P. Gao, M. K. Nazeeruddin, M. Gratzel, *Nature* **2013**, *499*, 316.

[3]   H. Zhou, Q. Chen, G. Li, S. Luo, T.-b. Song, H.-S. Duan, Z. Hong, J. You, Y. Liu, Y. Yang, *Science* **2014**, *345*, 542.

[4]   A. Mei, X. Li, L. Liu, Z. Ku, T. Liu, Y. Rong, M. Xu, M. Hu, J. Chen, Y. Yang, M. Grätzel, H. Han, *Science* **2014**, *345*, 295.

[5]   W. Liao, Y. Tang, P. Li, Y. You, R. Xiong, *J. Am. Chem. Soc.* **2017**, *139,* 18071.

[6]   Y. You, W. Liao, D. Zhao, H. Ye, Y. Zhang, Q. Zhou, X. Niu, J. Wang, P. Li, D. Fu, Z. Wang, S. Gao, K. Yang, J. Liu, J. Li, Y. Yan, R. Xiong, *Science* **2017**, *357*, 306.

[7]   I. Chung, B. Lee, J. He, R. P. H. Chang, M. G. Kanatzidis, *Nature* **2012**, *485*, 486.

[8]   W. S. Yang, B.-W. Park, E. H. Jung, N. J. Jeon, Y. C. Kim, D. U. Lee, S. S. Shin, J. Seo, E. K. Kim, J. H. Noh, S. I. Seok, *Science* **2017**, *356*, 1376.

[9]   https://www.nrel.gov/pv/assets/images/efficiency-chart.png.

[10]   N. J. Jeon, J. H. Noh, W. S. Yang, Y. C. Kim, S. Ryu, J. Seo, S. I. Seok, *Nature* **2015**, *517*, 476.

[11]   W. Nie, H. Tsai, R. Asadpour, J.-C. Blancon, A. J. Neukirch, G. Gupta, J. J. Crochet, M. Chhowalla, S. Tretiak, M. A. Alam, H.-L. Wang, A. D. Mohite, *Science* **2015**, *347*, 522.

[12]   F. Hao, C. C. Stoumpos, R. P. H. Chang, M. G. Kanatzidis, *J. Am. Chem. Soc.* **2014**, *136*, 8094.

[13]   W. Shockley, H. J. Queisser, *J. Appl. Phys.* **1961**, *32*, 510.

[14]   G. E. Eperon, T. Leijtens, K. A. Bush, R. Prasanna, T. Green, J. T.-W. Wang, D. P. McMeekin, G. Volonakis, R. L. Milot, R. May, A. Palmstrom, D. J. Slotcavage, R. A. Belisle, J. B. Patel, E. S. Parrott, R. J. Sutton, W. Ma, F. Moghadam, B. Conings, A. Babayigit, H.-G. Boyen, S. Bent, F. Giustino, L. M. Herz, M. B. Johnston, M. D. McGehee, H. J. Snaith, *Science* **2016**, *354*, 861.

[15]   Z. Yu, M. Leilaeioun, Z. Holman, *Nat. Energy* **2016**, *1*, 16137.

[16]   F. Hao, C. C. Stoumpos, D. H. Cao, R. P. H. Chang, M. G. Kanatzidis, *Nat. Photonics* **2014**, *8*, 489.

[17]   K. Shum, Z. Chen, J. Qureshi, C. Yu, J. J. Wang, W. Pfenninger, N. Vockic, J. Midgley, J. T. Kenney, *Appl. Phys. Lett.* **2010**, *96*, 221903.

[18]   Z. Chen, C. Yu, K. Shum, J. J. Wang, W. Pfenninger, N. Vockic, J. Midgley, J. T. Kenney, *J. Lumin.* **2012**, *132*, 345.

[19]   D. Zhao, Y. Yu, C. Wang, W. Liao, N. Shrestha, C. R. Grice, A. J. Cimaroli, L. Guan, R. J. Ellingson, K. Zhu, X. Zhao, R.-G. Xiong, Y. Yan, *Nat. Energy* **2017**, *2*, 17018.

[20]   C. Liu, W. Li, H. Li, C. Zhang, J. Fan, Y. Mai, *Nanoscale* **2017**, *9*, 13967.

[21]   J. Fan, C. Liu, H. Li, C. Zhang, W. Li, Y. Mai, *ChemSusChem* **2017**, *10*, 3839.

[22]   H. L. Zhu, J. Xiao, J. Mao, H. Zhang, Y. Zhao, W. C. H. Choy, *Adv. Funct. Mater.* **2017**, *27*, 1605469.

[23]   F. Hao, C. C. Stoumpos, P. Guo, N. Zhou, T. J. Marks, R. P. H. Chang, M. G. Kanatzidis, *J. Am. Chem. Soc.* **2015**, *137*, 11445.

[24]   W. Liao, D. Zhao, Y. Yu, C. R. Grice, C. Wang, A. J. Cimaroli, P. Schulz, W. Meng, K. Zhu, R.-G. Xiong, Y. Yan, *Adv. Mater.* **2016**, *28, * 9333*.

[25]   W. Liao, D. Zhao, Y. Yu, N. Shrestha, K. Ghimire, C. R. Grice, C. Wang, Y. Xiao, A. J. Cimaroli, R. J. Ellingson, N. J. Podraza, K. Zhu, R.-G. Xiong, Y. Yan, *J. Am. Chem. Soc. **2016, 138, 12360.*

[26]   J. Yao, T. Kirchartz, M. S. Vezie, M. A. Faist, W. Gong, Z. He, H. Wu, J. Troughton, T. Watson, D. Bryant, J. Nelson, *Phys. Rev. Appl.* **2015**, *4*, 014020.

[27] A. Rajagopal, Z. Yang, S. B. Jo, I. L. Braly, P.-W. Liang, H. W. Hillhouse, A. K. Y. Jen, *Adv. Mater.* **2017**, *29*, 1702140.

[28] P. L. Qin, G. Yang, Z. w. Ren, S. H. Cheung, S. K. So, L. Chen, J. Hao, J. Hou, G. Li, *Adv. Mater.* **2018**, *30*, 1706126.

[29] Q. Zeng, X. Zhang, X. Feng, S. Lu, Z. Chen, X. Yong, S. A. T. Redfern, H. Wei, H. Wang, H. Shen, W. Zhang, W. Zheng, H. Zhang, J. S. Tse, B. Yang, *Adv. Mater.* **2018**, *30*, 1705393.

[30] W. Zhao, D. Qian, S. Zhang, S. Li, O. Inganäs, F. Gao, J. Hou, *Adv. Mater.* **2016**, *28*, 4734.

[31] Y. Hou, X. Du, S. Scheiner, D. P. McMeekin, Z. Wang, N. Li, M. S. Killian, H. Chen, M. Richter, I. Levchuk, N. Schrenker, E. Spiecker, T. Stubhan, N. A. Luechinger, A. Hirsch, P. Schmuki, H.-P. Steinrück, R. H. Fink, M. Halik, H. J. Snaith, C. J. Brabec, *Science* **2017**, *358*, 1192

[32] Z. Zhu, Y. Bai, H. K. H. Lee, C. Mu, T. Zhang, L. Zhang, J. Wang, H. Yan, S. K. So, S. Yang, *Adv. Funct. Mater.* **2014**, *24*, 7357.

[33] Q. Jiang, L. Zhang, H. Wang, X. Yang, J. Meng, H. Liu, Z. Yin, J. Wu, X. Zhang, J. You, *Nat. Energy* **2016**, *2*, 16177.

[34] C. Bi, Q. Wang, Y. Shao, Y. Yuan, Z. Xiao, J. Huang, *Nat. Commun.* **2015**, *6*, 7747.

[35] Y. Li, Y. Zhao, Q. Chen, Y. Yang, Y. Liu, Z. Hong, Z. Liu, Y.-T. Hsieh, L. Meng, Y. Li, Y. Yang, *J. Am. Chem. Soc.* **2015**, *137*, 15540.

[36] Z. Liu, J. Hu, H. Jiao, L. Li, G. Zheng, Y. Chen, Y. Huang, Q. Zhang, C. Shen, Q. Chen, H. Zhou, *Adv. Mater.* **2017**, *29*, 1606774.

[37] W. Chen, J. Zhang, G. Xu, R. Xue, Y. Li, Y. Zhou, J. Hou, Y. Li, *Adv. Mater.* **2018**, *30*, 1800855.

[38] W. Q. Liao, D. W. Zhao, Y. Yu, N. Shrestha, K. Ghimire, C. R. Grice, C. L. Wang, Y. Q. Xiao, A. J. Cimaroli, R. J. Ellingson, N. J. Podraza, K. Zhu, R. G. Xiong, Y. F. Yan, *J. Am. Chem. Soc.* **2016**, *138*, 12360.

[39] K. J. H., L. Po‐Wei, W. S. T., C. Namchul, C. Chu‐Chen, G. M. S., G. D. S., J. A. K.‐Y., *Adv. Mater.* **2015**, *27*, 695.

[40] S. R. Cowan, A. Roy, A. J. Heeger, *Phys. Rev. B* **2010**, *82*, 245207.

[41] A. K. K. Kyaw, D. H. Wang, D. Wynands, J. Zhang, T.-Q. Nguyen, G. C. Bazan, A. J. Heeger, *Nano Lett.* **2013**, *13*, 3796.

[42]   H.-W. Lin, C.-W. Lu, L.-Y. Lin, Y.-H. Chen, W.-C. Lin, K.-T. Wong, F. Lin, *J. Mater. Chem. A* **2013**, *1*, 1770.

[43]   F. Fabregat-Santiago, G. Garcia-Belmonte, I. Mora-Sero, J. Bisquert, *Phys. Chem. Chem. Phys.* **2011**, *13*, 9083.

[44]   C. Liu, K. Wang, P. Du, C. Yi, T. Meng, X. Gong, *Adv. Energy Mater.* **2015**, *5*, 1402024.

[45]   C. Dan, J. F. C., W. Bright, N. Thuc‐Quyen, D. J. R., *Adv. Mater.* **2012**, *24*, 2135.

[46]   Q. Xue, G. Chen, M. Liu, J. Xiao, Z. Chen, Z. Hu, X.-F. Jiang, B. Zhang, F. Huang, W. Yang, H.-L. Yip, Y. Cao, *Adv. Energy Mater.* **2016**, *6*, 1502021.

[47]   H. Dong, Z. Wu, J. Xi, X. Xu, L. Zuo, T. Lei, X. Zhao, L. Zhang, X. Hou, A. K. Y. Jen, *Adv. Funct. Mater.* **2018**, *28*, 1704836.

[48]   A. Poglitsch, D. Weber, *J. Chem. Phys.* **1987**, *87*, 6373.

[49]   N. Zhou, Y. Shen, Y. Zhang, Z. Xu, G. Zheng, L. Li, Q. Chen, H. Zhou, *Small* **2017**, *13*, 1700484.

[50]   J. Jiang, Q. Wang, Z. Jin, X. Zhang, J. Lei, H. Bin, Z.-G. Zhang, Y. Li, S. Liu, *Adv. Energy Mater.* **2018**, *8*, 1701757.

[51]   K. Chen, P. Wu, W. Yang, R. Su, D. Luo, X. Yang, Y. Tu, R. Zhu, Q. Gong, *Nano Energy* **2018**, *49*, 411.

[52]   J. Haruyama, K. Sodeyama, L. Han, Y. Tateyama, *J. Phys. Chem. Lett.* **2014**, *5*, 2903.

[53]   A. Buin, P. Pietsch, J. Xu, O. Voznyy, A. H. Ip, R. Comin, E. H. Sargent, *Nano Lett.* **2014**, *14*, 6281.

[54]   Z. Qingsen, Z. Xiaoyu, F. Xiaolei, L. Siyu, C. Zhaolai, Y. Xue, R. S. A. T., W. Haotong, W. Haiyu, S. Huaizhong, Z. Wei, Z. Weitao, Z. Hao, T. J. S., Y. Bai, *Adv. Mater.* **2018**, *30*, 1705393.

Table of Content

We developed a facile way to address the bottleneck of high E_{loss} of low bandgap perovskite solar cells (pero-SCs) by incorporating an ultra-thin BHJ organic semiconductors (PBDB-T:ITIC) intermediary. The resulting Sn-Pb-based pero-SCs showed the highest reported efficiency of 18.03% in the low-bandgap (below 1.4 eV) pero-PCs to date.

*Guiying Xu, [a] Pengqing Bi, [c] Shuhui Wang, [a] Rongming Xue, [a] Jingwen Zhang, [a] Haiyang Chen, [a] Weijie Chen, [a] Xiaotao Hao, [c] Yaowen Li, [*a] Yongfang Li [a,b]*

Guiying Xu, Shuhui Wang, Rongming Xue, Jingwen Zhang, Haiyang Chen, Weijie Chen, Prof. Yaowen Li,* Prof. Yongfang Li

[a] *State and Local Joint Engineering Laboratory for Novel Functional Polymeric Materials, Laboratory of Advanced Optoelectronic Materials, College of Chemistry, Chemical Engineering and Materials Science, Soochow University, Suzhou 215123, China*
Prof. Yaowen Li *Email: ywli@suda.edu.cn*

Prof. Yongfang Li

[b] *Beijing National Laboratory for Molecular Sciences; Institute of Chemistry, Chinese Academy of Sciences, Beijing 100190, China*

Prof. Xiaotao Hao, Pengqing Bi

[c] *School of Physics and State Key Laboratory of Crystal Materials, Shandong University, Jinan, Shandong 250100, China*

Integrating Ultra-thin Bulk-heterojunction Organic Semiconductor Intermediary for High-performance Low-bandgap Perovskite Solar Cells with Low Energy Loss

$(FASnI_3)_{0.6}(MAPbI_3)_{0.4}$

$E_{loss} = 0.39$ eV

PCE = 18.03% J_{sc} = 27.92 mA/cm²
FF = 0.751 V_{oc} = 0.86V
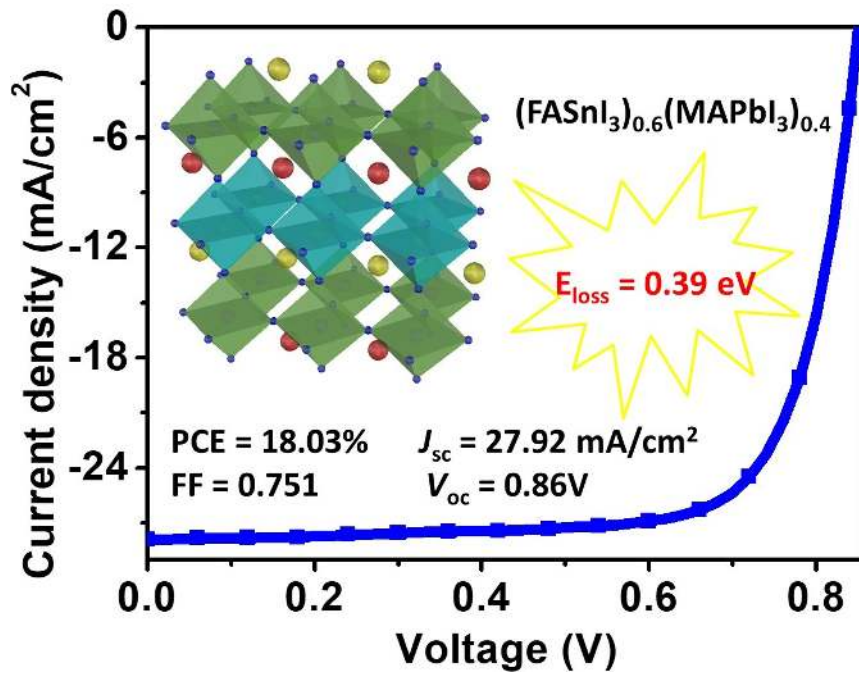
Author/s:
Xu, G;Bi, P;Wang, S;Xue, R;Zhang, J;Chen, H;Chen, W;Hao, X;Li, Y;Li, Y

Title:
Integrating Ultrathin Bulk-Heterojunction Organic Semiconductor Intermediary for High-Performance Low-Bandgap Perovskite Solar Cells with Low Energy Loss

Date:
2018-10-17

Persistent Link:
http://hdl.handle.net/11343/284536